Inorganic Chemistry

pubs.acs.org/IC Article

Noncovalent Dualism in Perylene-Diimide-Based Keggin Anion Complexes: Theoretical and Experimental studies

Victoria G. Popova, Leonid V. Kulik, Rimma I. Samoilova, Dmitri V. Stass, Vasily V. Kokovkin, Evgeni M. Glebov, Alexey S. Berezin, Alexander S. Novikov, Aura Garcia, Hoang Tran Tuan, Raul D. Rodriguez, Maxim N. Sokolov, and Pavel A. Abramov*

Cite This: *Inorg. Chem.* 2023, 62, 19677−19689

ABSTRACT: We report the synthesis and comprehensive characterization of organic−inorganic hybrid salts formed by bis-cationic *N*,*N*′-bis(2-(trimethylammonium)ethylene)perylene-3,4,9,10-tetracarboxylic acid bisimide ($PTCD^{2+}$) and Keggin-type $[XW_{12}O_{40}]^{n-}$ (X = Si, *n* = 4; X = P, *n* = 3) polyoxometalates. $(PTCD)_3[PW_{12}O_{40}]_2 \cdot 3DMSO \cdot 2H_2O$ (**2**) and $(PTCD)_2[SiW_{12}O_{40}] \cdot DMSO \cdot 2H_2O$ (**3**) were structurally characterized by single crystal X-ray diffraction. The cations in both structures exhibited infinite chainlike arrangements through *π*−*π* interactions, contrasting with the previously reported cation−anion stacking observed in naphthalene diimide derivatives. A detailed theoretical study employing topological analysis of the electron density distribution within the quantum theory of atoms in molecules approach provided further insights into this structural dualism. Atomic force microscopy analyses revealed the formation of self-assembled supramolecular structures on graphite from molecular monolayers (3 nm of thick) to submicrometer aggregates for **2**. Hyperspectral Raman spectroscopy imaging revealed that such heterostructures are likely formed by an enhanced *π*−*π* interactions. Both complexes demonstrated interesting electrochemical behavior, photoluminescence and X-ray-induced luminescence. Electron spin resonance analysis confirmed charge separation in both compounds, with enhanced efficiency observed in compound **2**. Our findings of these perylene-based organic−inorganic hybrid salts offer the potential for their application in optoelectronic devices and functional materials.

■ INTRODUCTION

Interfacial layers between the active media and the electrodes play a crucial role in modern solar energy conversion devices, such as organic, perovskite,[1,2] and dye-sensitized solar cells.[3] The optimization of these active media often faces limitations in power conversion efficiency due to nonselective charge extraction to the electrodes and the mismatch in work function between the active material and electrode.[4]

To address these challenges, polyoxometalates (POMs) were put forward as promising materials for both cathode interlayers[5−8] and for hole transporting layers (anode interlayer)[9] in organic photovoltaic (OPV) devices. Besides, POMs have demonstrated their potential in improving the performance of dye-sensitized solar cells,[10] perovskite solar cells, and energy storage devices.[11]

POM anionic backbones possess unique characteristics that make them ideal for studying charge transfer and separation as well as for various applications. One key point is the presence of a large number of reducible metal ions in their highest oxidation state, enabling multielectron reduction. For instance, the Keggin $[XW_{12}O_{40}]^{n-}$ backbone can accommodate up to 24 additional electrons without undergoing structural changes.[12] Redox activating POM molecules requires inducing charge transfer to the POM through excitations such as visible light,[13−15] voltage,[16] or even X-ray photons.[17] The main challenge in this field concerns the design and fabrication of memory devices,[18] and the enhancement of photocatalytic activity. For example, Bonchio et al. reported a remarkable photocatalytic activity of bis-cationic *N*,*N*′-bis(2-(trimethylammonium)ethylene)perylene-3,4,9,10-tetracarboxylic acid bisimide/$[Ru_4(\mu\text{-}O)_4(\mu\text{−}OH)_2(H_2O)_4(\gamma\text{-}SiW_{10}O_{36})_2]^{10-}$ system for photoassisted water oxidation.[19] POM-based hybrids with specific organic cations are the most preferable for constructing high-performance and sustainable charge transfer/separation systems, particularly within different photovoltaic devices.[10] Vasilopoulou et al. applied POMs as

Received: August 30, 2023
Revised: November 2, 2023
Accepted: November 10, 2023
Published: November 17, 2023

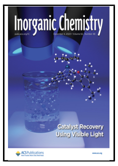

https://doi.org/10.1021/acs.inorgchem.3c03030
Inorg. Chem. 2023, 62, 19677−19689

electron injection layers in organic solar cells, leading to improved efficiency and stability in numerous studies.[4,5,20,21]

The chemistry of rylene diimides has garnered strong and growing interest, particularly due to their photochemical and electrochemical activity.[22,23] For example, naphthalene diimides (NDI) and perylene diimides (PDI), the two simplest rylene diimide dyes, have been recognized as the most promising n-type organic semiconducting materials.[24,25] This vibrant research field combines organic synthesis with materials science to explore potential applications of rylene diimides. Rylene diimides have great thermal and oxidative stability, high electron affinities, and, in many cases, high electron mobilities.[26] Combining POMs with rylene diimides holds great potential for creating a new generation of materials with diverse applications in photovoltaics, catalysis, electronics, and more. The interest for such compounds has been increasing steadily since the publications by Can-Zhong Lu et al. describing $[Cr(H_2O)_3(H_3O)_3][DPNDI]_3[PW_{12}O_{40}]_2\cdot$nSovlent HOF[27] and photochromism of $[Cu_2(DPNDI)_2(H_2O)_7(OH)(PW_{12}O_{40})]_n$ and $[Cu[(DPMNI)(C_4H_9NO)_2(CH_3OH)(HPW_{12}O_{40})]_n$ (DPNDI = *N,N′*-di(4-pyridyl)-1,4,5,8-naphthalenediimide; DPMNI = *N,N′*-bis(4-pyridylmethyl)-1,4,5,8-naphthalenediimide).[28] Keggin POM salts with protonated *N,N′*-dipyridyl naphthalene diimide (DPyNDI)[29] and *N,N′*-bis(3,5-dimethylpyrazolyl)-2,6-dibromo/iodo-1,4,5,8-naphthalene diimide[30] have been structurally characterized. Cheng et al. reported an organic−inorganic hybrid compound, $[Ce_2(BINDI)(DMF)_8][Mo_6O_{19}]$ (**1**), (H_4BINDI = *N,N′*-bis(5-isophthalic acid)-1,4,5,8-naphthalene diimide) as a self-assembly product of an electron-deficient NDI ligand, Ce^{3+} and hexamolybdate.[31] All the reported complexes were summarized in the review by Mei-Jin Lin et al. as photochromic crystalline hybrid materials with switchable properties.[32] The main structural feature of such compounds is direct anion-π contacts, which can be responsible for their photochromic behavior.

It is widely accepted that noncovalent interactions have a great potential in POMs' chemistry for the new materials design.[33] The main construction vector is based on the electronic pool around terminal oxoligands, which can interact with a huge number of σ-hole owners. Halogen bonding is one of the most promising instruments in this field of research.[34−37] Some years ago, we reported a set of compounds when Mo═O•••X (X = Cl, Br, I) halogen bonding do organize $[\beta\text{-}\{Ag(py\text{-}X)\}_2Mo_8O_{26}]^{2-}$ anions into specifically ordered supramolecular structures in the solid state.[38] Recently Stilinović et al. analyzed halogen bonding between Keggin anions and some halogenated organic moieties.[39]

The goal of this study was to investigate a new type of organic−inorganic hybrid materials by combining Keggin anions with a bis-cationic *N,N′*-bis(2-(trimethylammonium)-ethylene)perylene-3,4,9,10-tetracarboxylic acid bisimide (Figure 1) based on noncovalent interactions.

■ RESULTS AND DISCUSSION

Synthesis and Structure. The hybrid salts of $[XW_{12}O_{40}]^{n-}$ (X = P, *n* = 3; X = Si, *n* = 4) and $PTCD^{2+}$ were obtained through the direct reaction between the corresponding POM acids and $PTCDI_2$ (**1**) (see the Experimental section in the SI). The most suitable solvents for these salts were found to be dimethyl sulfoxide (DMSO) and *N,N*-dimethylformamide (DMF). Crystalline materials suitable for single crystal X-ray diffraction (SCXRD) analysis were obtained by the slow diffusion of the reactants through H-tubes in DMSO.

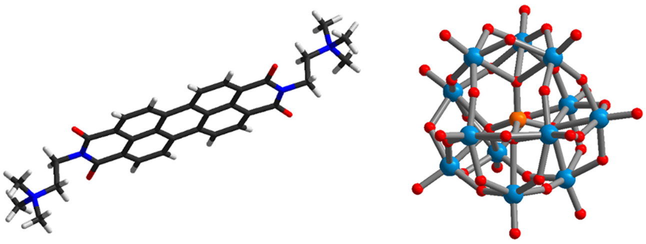

Figure 1. (left) Structure of $PTCD^{2+}$ (N is blue, O is red, C is black); (right) Keggin type anion (M atoms are blue, oxoligands are red, and central heteroatom is orange).

In the case of $H_3[PW_{12}O_{40}]$ and $PTCD^{2+}$, the resulting product crystallized in a triclinic crystal system with the *P*−1 space group (Figure 1), exhibiting the following unit cell parameters: *a* = 11.4179(6), *b* = 17.7695(9), *c* = 27.5053(15) Å, α = 104.640(2)°, β = 95.868(2)°, and γ = 98.835(2)°. The crystal structure revealed that $PTCD^{2+}$ cations form infinite columns via $\pi-\pi$ interactions, with an approximate carbon-to-carbon distance (d(C···C)) of 3.5 Å (Figure 2).

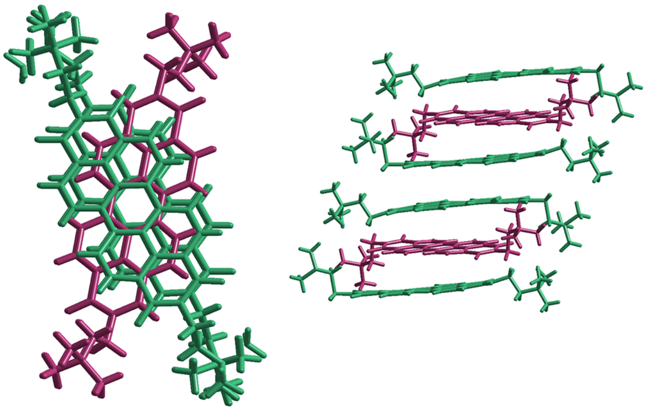

Figure 2. Stacking of $\mathbf{PTCD^{2+}}$ cations in the crystal structure of **2**. Two types of cations are marked in green and purple correspondingly.

A notable feature is the nonlinear orientation of dications within the $\pi-\pi$ stacked chains (Figure 2). The stacking arrangement can be described as ABAABAA, where associates consisting of three dications translate via an inversion center symmetry operator in the crystal. This stacking pattern can be very interesting from a conductivity point of view, which has been extensively studied in the context of perylene-based materials.[40−44] In silico studies by Geng et al.[45] investigated carrier transport in perylene-based materials and have specifically studied the angle between the molecule axes. In our case, this angle is close to 40°, which prevents electron transfer but may be favorable for hole transfer within the stacked molecules.

It is intriguing to compare our chain structure with those found in perylene-radical salts containing $[PMo_{12}O_{40}]^{3-}$.[46] For instance, in the structure of $Per_6[PMo_{12}O_{40}]\cdot CH_2Cl_2$, perylene molecules form two types of chains following the ABBA pattern, while the structure of $Per_9(NBu_4)_4[SiW_{12}O_{40}]_2$ reveals more complex chains with CBAAB stacking. This implies that the presence of column aggregates with different molecular

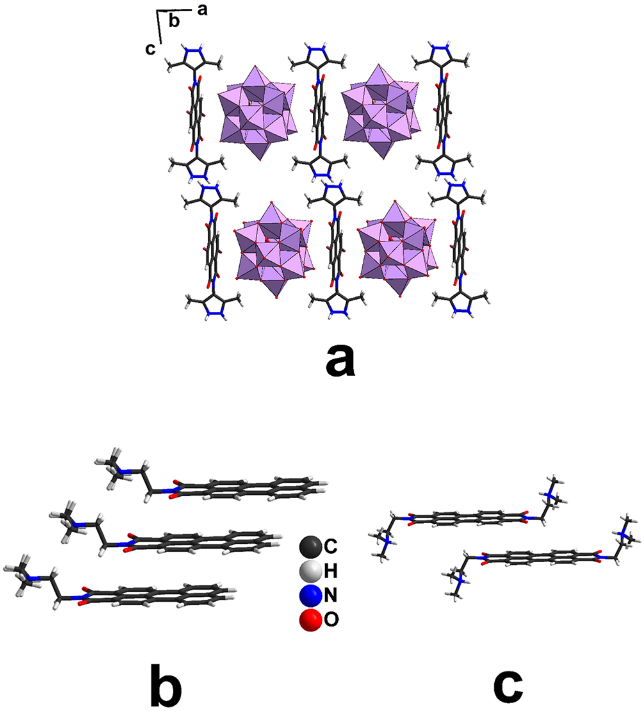

Figure 3. Main packing motif of **2085758**, **2085793** (a); **per_Et2** (b), and **per_Me2** (c).

orientations is preferable for stabilizing the radical state (POMs are not reduced; Per^{+}● are located inside the π-stacked chains). Hence, a similar effect could be proposed for our complexes.

In the case of $H_4[SiW_{12}O_{40}]$, the $PTCD^{2+}$ salt crystallizes in a triclinic crystal system with unit cell parameters: a = 14.086(7), b = 29.668(14), c = 50.83(3) Å, α = 103.42(3), β = 93.89(3), and γ = 100.53(3)°. The crystal structure exhibits two independent Keggin anions located in common and special positions (an inversion center is at the center of an anion). Strong stacking interactions (d(C●●●C) = 3.6−3.7 Å) form infinite chains of $PTCD^{2+}$ cations. However, the quality of the crystalline material was insufficient to reach an appropriate diffraction limit. Consequently, we present a tentative model of the structure at this stage, with the detailed SCXRD data available in the SI (see the Crystallography section). Based on the analytical data for a dried sample, the overall composition can be formulated as $(PTCD)_2[SiW_{12}O_{40}]\cdot DMSO\cdot 2H_2O$ (**3**).

The space between $PTCD^{2+}$-based chains and Keggin anions is filled with DMSO molecules. The final refinement process localized 12 DMSO molecules per formula unit for **2**. It is important to note that the isolated product is always wet and cannot be readily manipulated. To obtain more manageable compounds, we treated these solids with acetone and diethyl ether (Et_2O). Elemental analysis of the dried products confirmed the composition of $(PTCD)_3[PW_{12}O_{40}]_2\cdot 3DMSO\cdot 2H_2O$ (**2**) and $(PTCD)_2[SiW_{12}O_{40}]\cdot DMSO\cdot 2H_2O$ (**3**). These materials were subsequently used for further studies.

Structural Dualism. A recent study by Lin et al.[30] focused on hybrid crystals, namely, $(H_4BDMPy\text{-}Br_2NDI)[HPW_{12}O_{40}]\cdot 4NMP$ (CCDC **2085758**) and $(H_4BDMPy\text{-}I_2NDI)[HPW_{12}O_{40}]$ (CCDC **2085793**) ($H_2BDMPy\text{-}Br_2NDI$: *N*,*N*′-bis(3,5-dimethylpyrazolyl)-2,6-dibromo-1,4,5,8-naphthalenediimide and $H_2BDMPy\text{-}I_2NDI$: *N*,*N*′-bis(3,5-dimethylpyrazolyl)-2,6-diiodide-1,4,5,8-naphthalenediimide). In both structures, the crystal packing is dominated by close cation−anion interactions (Figure 3a) analogously to previously reported salts involving protonated *N*,*N*-dipyridyl naphthalene diimide (DPyNDI) and Keggin anions.[29]

In contrast, it is well known that large aromatic systems have a tendency to exhibit multiple stacking interactions.[47−49] Thus, the preferential formation of the aforementioned anion−π interactions can be attributed to the predominance of multiple C−O binding over bulk π−π stacking. To analyze these contacts, we employed quantum chemical calculations. For comparison, we considered the structures of N-(2-(diethylamino)ethyl)perylene-3,4-dicarboximide[50] (CCDC 632620, **per_Et2**), and 2,2′-(1,3,8,10-tetraoxo-1,3,8,10-tetrahydroisoquinolino[4′,5′,6′:6,5,10]anthra[2,1,9-def]-isoquinoline-2,9-diyl)bis(N,N-dimethylethan-1-aminium) bis(hexafluorophosphate)[51] (CCDC 1952503, **per_Me2**). The stacking arrangements in these structures are shown in Figure 3b,c correspondingly. π−π interactions found with PLATON in the crystal structure of **2** are summarized in Table S5.

To investigate the presence and strength of intermolecular interactions involving O···C and C···C in the X-ray structures **2085758**, **2085793**, complex **2**, **per_Et2**, and **per_Me2**, theoretical calculations were performed using DFT coupled with the topological analysis of the electron density distribution within the Quantum Theory of Atoms in Molecules (QTAIM) approach.[52] These calculations were carried out at the ωB97XD/DZP-DKH level of theory for model structures (see the Computational Details in the Supporting Information). Additionally, contour line diagrams of the Laplacian of electron density distribution $\nabla^2\rho(\mathbf{r})$, bond paths, and selected zero-flux surfaces, as well as visualization of the electron localization function (ELF) and reduced density gradient (RDG) analyses for selected intermolecular interactions O···C and C···C in the X-ray structures **2085758** and complex **2**, respectively, are shown in Figure 4. These analyses aimed to confirm or refute the hypothesis and provide an approximate quantification of the strength of these supramolecular contacts from a theoretical perspective.

The QTAIM analysis of the model structures confirms the presence of bond critical points (3, −1) for the intermolecular interactions O···C and C···C in the X-ray structures **2085758**, **2085793**, complex **2**, **per_Et2**, and **per_Me2** (Table S6). The electron density values at these bond critical points are from 0.003 to 0.011 atomic units, with positive values of the Laplacian of electron density (0.011−0.046 atomic units) and energy density close to zero (0.001−0.002 au). These characteristics, along with the estimated strength of the short contacts, ranging from 0.3 to 2.2 kcal/mol per contact, are typical for stacking interactions in similar chemical systems.[33,53−60] The balance between the Lagrangian kinetic energy $G(\mathbf{r})$ and potential energy density $V(\mathbf{r})$ at the bond critical points (3, −1) (with a ratio $-G(\mathbf{r})/V(\mathbf{r}) > 1$) reveals the absence of a significant covalent contribution in the intermolecular interactions O···C and C···C within the X-ray structures **2085758**, **2085793**, complex **2**, **per_Et2**, and **per_Me2**.[61] (Table S6). The Laplacian of electron density, which can be decomposed into the three eigenvalues of the Hessian matrix (λ_1, λ_2, and λ_3), shows that the intermolecular interactions O···C and C···C are attractive ($\lambda_2 < 0$).[62,63]

The comparison of energetics gives very interesting results. The energy of cation−anion interactions in **2085758** and **2085793** slightly exceeds the energy of π−π interactions in

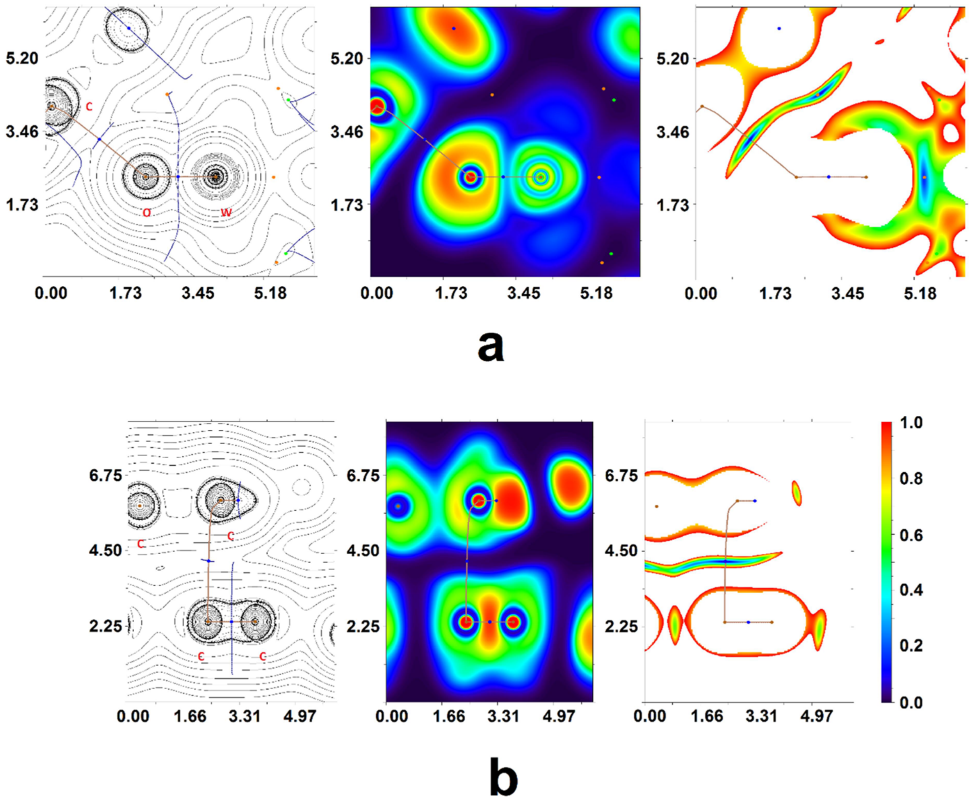

Figure 4. Computational data for complex **2085758** (a) and complex **2** (b). Bond critical points (3, −1) are shown in blue, nuclear critical points (3, −3) in pale brown, ring critical points (3, +1) in orange, cage critical points (3, +3) in light green, bond paths are shown as pale brown lines, length units − Å, and the color scale for the ELF and RDG maps are presented in a.u.

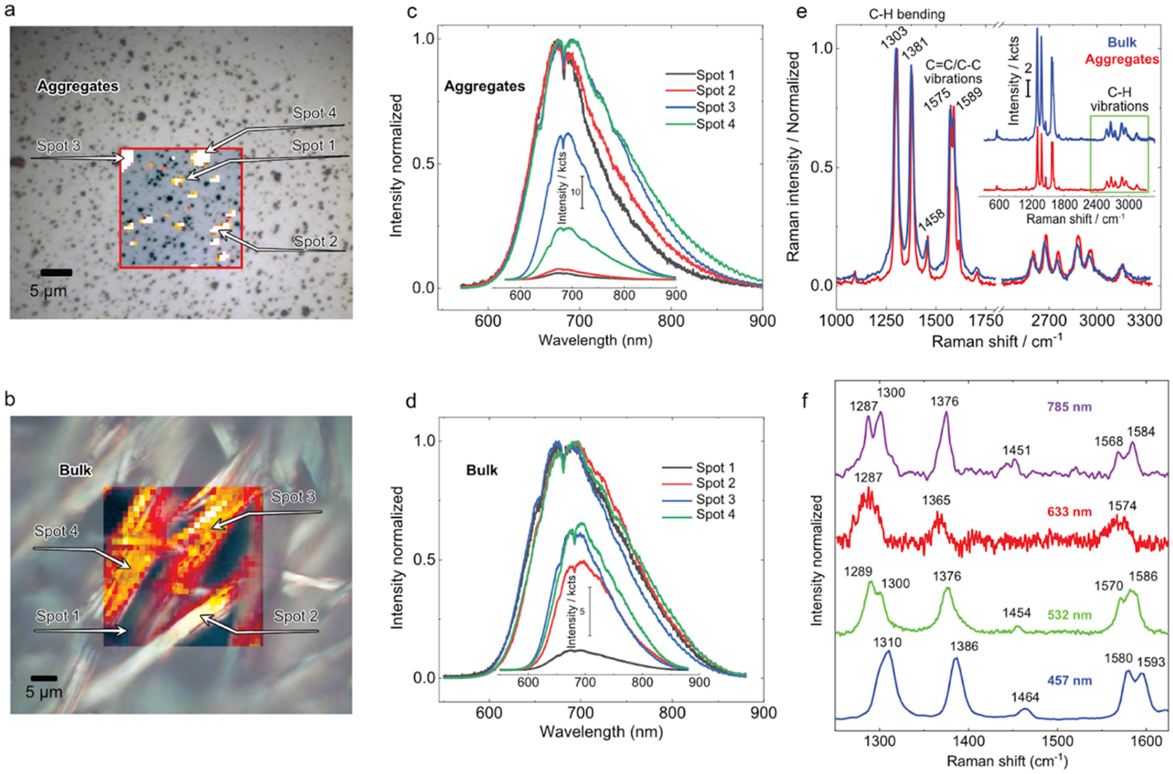

Figure 5. Photoluminescence maps overlaid on the optical microscopy image of the complex **2** sample deposited on graphite (a) and the bulk sample (b); (c, d) normalized PL spectra extracted from representative points on the maps in (a) and (b) labeled 1−4. The insets show the non-normalized spectra; (e) normalized Raman spectra from one aggregate in (a) and the bulk in (b). The inset shows the non-normalized spectra; (f) Raman spectra obtained at different excitation wavelengths.

per_Et2 and **per_Me2** related systems. This preference for the formation of crystal packing is observed when cations strongly bind to the Keggin anions, while in the case of complex **2**, this situation switches to $\pi-\pi$ interactions. This dualism in the packing motif is significant for such compounds and has a strong effect on the electronic properties of the bulk material. To illustrate this, we performed detailed studies on the PL, electrochemical behavior, Raman spectroscopy, electrical atomic force microscopy, and ESR activity of presented complexes formed by $PTCD^{2+}$ with Keggin anions.

Photoluminescence and Raman Spectroscopy: Influence of the Aggregation State and Packing Density. To obtain more details on the material capability for the photogeneration of charge carriers, we investigated its photoluminescence (PL) spectra under different wavelengths and with spatially resolved hyperspectral PL imaging. Figure 5a, b show the PL emission intensity maps overlapped with optical microscopy images for complex **2** deposited on graphite and the bulk sample, respectively. The normalized PL spectra extracted from representative points on the photoluminescence maps are shown in Figure 5c, d. First, the microscopy images show the circular shape of nanoparticles from the bulk sample dispersed in acetone. Meanwhile, the bulk as-prepared sample shows an anisotropic needle-like morphology (Figure 5b). The PL results show two strong emission bands at 675 and 687 nm, indicating efficient radiative decay of the excited state. The peak at 687 nm is due to the fast recombination of excited electrons and holes in the sample.[64] While the bulk sample shows PL spectra from different locations that overlap (Figure 5d), the aggregates show some dispersion toward longer wavelengths. This phenomenon can be attributed to aggregation state and packing density within the respective samples. Micrometer-sized samples displayed a tendency for aggregation or clustering at the microscopic level, leading to the formation of varied aggregated configurations, each contributing to a unique electronic environment. Consequently, the excited states of these aggregates exhibit diverse energy levels, resulting in a broader spectrum of emitted light, as shown in Figure 5b.

Notably, we do not observe the typical emission quenching for PDI aggregates in the solid state,[65] which we attribute to the noncovalent interaction with the Keggin anions.

Raman spectroscopy of PDI on freshly cleaved highly oriented pyrolytic graphite (HOPG) was performed with a blue laser (457 nm) with a maximum power of 452 μW and an exposure time of 0.2 s. The resulting spectrum showed characteristic PDI vibrational modes at 1310, 1386, 1464, 1580, and 1593 cm^{-1}, as shown in Figure 5e.

The peaks at 1580 and 1593 cm^{-1} correspond to the stretching/shrinking vibration of planar C=C/C−C in the PDI molecule.[64,66] This vibration is coupled to the C=O antisymmetric stretching and is influenced by the $\pi-\pi$ stacking interactions. On the other hand, the peak at 1310 cm^{-1} assigned to C−H in-plane bending is not sensitive to the $\pi-\pi$ stacking interaction, but other noncovalent interactions may contribute to binding force.[64,66] The peak intensity ratio between 1593 and 1310 cm^{-1} can be used to quantify the degree of $\pi-\pi$ stacking interaction in the system.[64] In this study, the ratio value of 0.67 implies a high degree of $\pi-\pi$ stacking interaction between the aromatic rings, which should translate to improved carrier mobility. This value is higher than the optimized 0.56 from phosphoric acid-substituted perylene diimide.[64] This is a critical result since the photocatalytic material's optical and electronic properties depend on the stacking degree. The peak at 1707 cm^{-1} corresponds to the C=O stretching mode,[67] while the peaks in the region 2600−3200 (besides the 2D from the carbon substrate) are assigned to the C−H stretching vibrational modes.[68] The intensity in this high-frequency window can be attributed to stronger adsorption energies.[69]

The vibrational modes under different excitation wavelengths are shown in Figure 5f. The Raman spectra were obtained using 457 nm (452 μW), 532 nm (389 μW), 633 nm (1.3 mW), and 785 nm (1 mW). The Raman peaks were observed to downshift with an increasing laser wavelength. This dispersive behavior is unusual in Raman and can be attributed to the coupling between the electronic and vibrational energy states in complex **2**. The peak around 1300 cm^{-1} exhibited an intriguing behavior. This peak, attributed to C−C stretching and CH in-plane bending, split into two distinct peaks under 785 and 532 nm excitation wavelengths, indicating resonance enhancement. However, this splitting phenomenon was not observed under 633 or 457 nm excitation, suggesting that the system did not show resonant absorption under these photon energies. This observation is confirmed by UV−vis spectroscopy results (Figure S11) showing a dip in the absorption at 450 nm and low absorption at 633 nm, which also explains why the Raman spectrum under this excitation wavelength was noisier than the others. This observation points toward a selective resonance response of the molecule's vibrational modes, highly dependent on the excitation wavelength used.

Both complex **2** and complex **3** exhibit temperature-dependent luminescence in bulk, and the emission increases at low temperatures (Figure S10). The nature of these transitions is complex and can tentatively be attributed to intermolecular electron transfer involving the cation and anion species. The excitation and emission profiles are related to well-known features of perylene diimide dyes.[65,70,71] However, the luminescence intensity of complex **3** is much lower compared to complex **2**. Therefore, the excited state is more energetically preferable for luminescence in the case of **2**. $(H_4BDMPy\text{-}Br_2NDI)[HPW_{12}O_{40}]\cdot 4NMP$ and $(H_4BDMPy\text{-}I_2NDI)[HPW_{12}O_{40}]$ show the same luminescence maxima at 670 nm,[30] indicating that the $[PW_{12}O_{40}]^{3-}$ anion favors PL in all cases. This observation suggests the potential use of these hybrids as active layers in optoelectronics. The diffuse reflectance spectra of bulk **2** and **3** are shown in Figure S11. Interestingly, a reversible narrowing of the band gap value is observed for complex **2**, decreasing from 2.0 to 1.95 eV when samples are warmed from −175 to 60 °C. For complex **3**, the band gap decreases from 1.91 to 1.88 eV from −175 to 80 °C (Figures S12 and S13).

Additionally, X-ray-induced photoluminescence spectra were measured for the polycrystalline samples of complex **2** and complex **3**, and the results can be found in Figure S14. We observed that complex **3** produces a moderate emission with a peak near 720 nm, which is strongly red-shifted compared to the light-induced PL (Figure S7). In contrast, complex **2** does not show any X-ray-induced luminescence. This difference can be attributed to the distinct nature of the exited states.

Nanoscale Characterization with Kelvin Probe and Dielectric Force Microscopy. We realized that the salt makes structures with different degrees of aggregation on HOPG from optical microscopy images obtained during Raman and photoluminescence spectroscopy. An example of

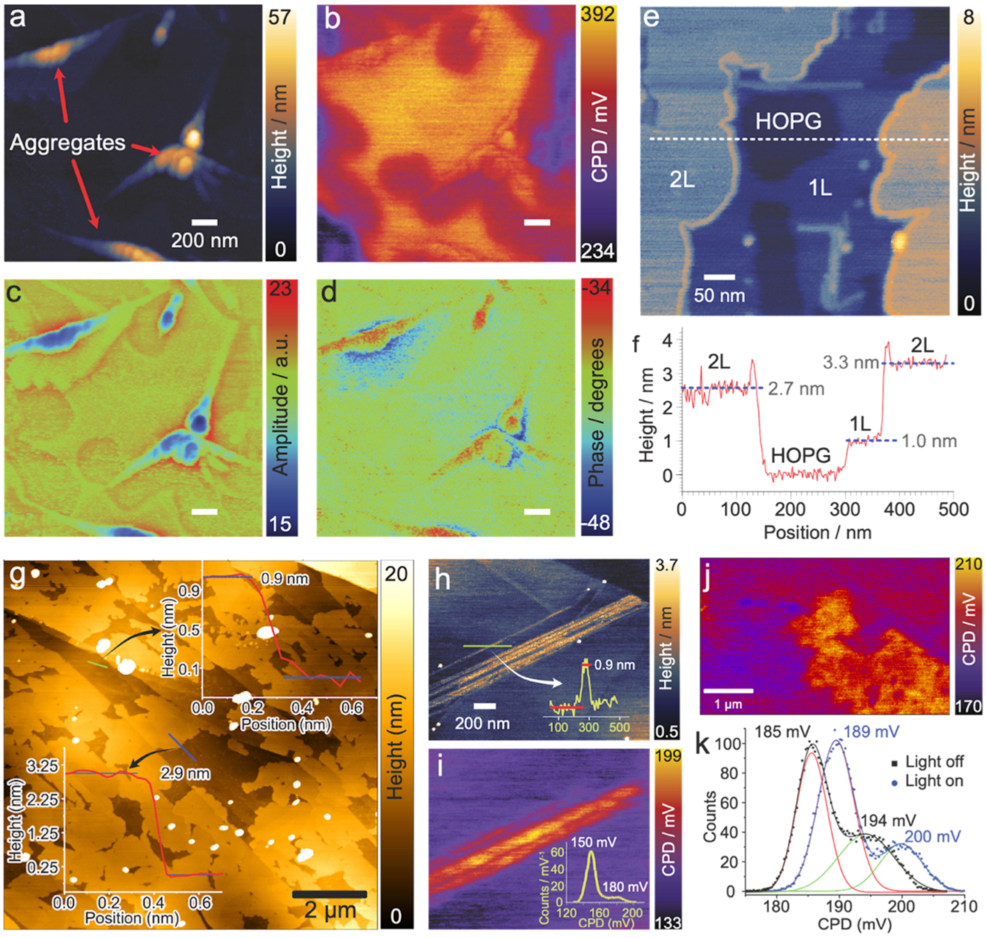

Figure 6. (a) Topography image of a concentrated region showing aggregates. The surface potential image (b) shows that these aggregates are deposited on 2D layers of complex **2**; (c) dielectric force microscopy amplitude and (d) phase images; (e) zoom-in over the 2D regions without aggregates and (f) cross-section profile showing the monolayer and bilayer thickness of complex **2** self-assembled on HOPG; (g) AFM image of the layered complex with cross-section profiles included as insets; (h) topography and (i) surface potential image of nanoribbons; (j) the surface potential of a monolayer complex; and (k) the surface potential distribution of monolayer complex on HOPG with and without illumination.

these aggregates is shown in Figures 6a and S9. The contact potential difference image acquired simultaneously with the topography mapping by Kelvin probe force microscopy is shown in Figure 6b. The CPD contrast shows that the aggregates coexist with a molecular carpet with the same surface potential as the aggregates. The HOPG CPD contrast appears in purple and red color. This suggests that the material making up the aggregates and the 2D film is made of the same component. Since we could see these self-assembly monolayers with an optical microscope, we confirmed their same composition by Raman spectroscopy (see Figure S9). The dielectric force microscopy result in Figure 6c shows a marked contrast between the 2D assemblies and the aggregates.

Moreover, since the amplitude is related to the local electrical conductivity, the contrast between the 2D layers and HOPG implies a high conductivity for these layers. This observation is in agreement with the Raman spectroscopy results that indicated a significant degree of $\pi-\pi$ coupling in this complex, which favors charge carrier mobility. However, the aggregates show a poorer conductivity which might be attributed to their larger size and charge scattering at different domain interfaces within the aggregates.

The DFM phase image in Figure 6d is related to the charge carrier doping type. Using HOPG as a reference for a rich electron system due to its pure sp^2 hybridization, we conclude that the 2D films with the same phase contrast must have n-type characteristics typical for PDI. Thus, this result confirms the noncovalent interaction with the Keggin salt that did not disrupt PDI electronic type, for instance, through doping.

We were curious about the formation of these 2D assemblies and thus acquired a high-resolution AFM image in a region without aggregates, as shown in Figure 6e. These layers are characterized by a highly uniform thickness characteristic of a self-assembly process. We attribute the monolayer and bilayer formation to the $\pi-\pi$ interaction between HOPG and perylene. The 2D bilayer (2L) structures in Figure 6e show different heights for the left and right sides: 2.7 and 3.3 nm, respectively. These 2L thickness values are not twice the monolayer measured at 1.0 nm, which means that the previous layer affects the packing and conformation of the next layer on top (that is why 2L has 3-fold the thickness of 1L), but also the 2L at the right side with 0.5 nm higher than the 2L at the right side, could suggest that the assembly is not unique and can result with domain layers with different thicknesses.

Figure 6g presents the topography characterized by monolayers and bilayers of 0.9 and 2.9 nm thick, respectively. These results are in good agreement with the AFM observations in Figure 6e, which were a different sample, showing the reproducibility of this result. Going farther away from the large aggregates, we find regions with lower complex

2 concentrations that formed nanoribbons (needle-like) structures like in Figure 6h. The cross-section profile of an individual nanoribbon in the inset of the figure shows that it has a height matching the 0.9 nm of the 2D monolayer $PTCD^{2+}$ ions.

Given that the sample diluted in acetone was deposited by drop casting on graphite, there was a radial concentration gradient from the edge of the drop toward the middle as the drop dried. This explains why over the whole sample we observed different shapes, including aggregates, 2D layers, and nanoribbons, spanning sizes from the monolayer to the submicrometer level (see also Figure S9). This is an exciting result since controlling the size complex range to the nanoscale is critical for catalysis and sensing applications with more active sites becoming accessible with size decrease and also the electron−ion pathway becomes shorter. This size and morphology control can be easily achieved by controlling complex **2** concentration.

Figure 6i shows the surface potential image of the nanoribbon, showing a significant contrast with the HOPG substrate, as illustrated by the CPD distribution in the inset.

We also investigated the effect of light on the surface potential values in photo-KPFM; see the results in Figure 6j. However, we do not see significant changes in CPD (about 5 mV) to positive values, as shown in the CPD distribution in Figure 6k, corresponding to net positive charging (compensation bias applied to the sample). A close inspection of this result shows that the CPD contrast of HOPG shifted to larger values. We attribute this shift to the electrostatic, mechanical, and photoinduced disruption of the 2D layers that result in the diffusion of molecules all over the HOPG substrate affecting its surface potential. Although this result requires further investigation, it was interesting to verify at the nanoscale the light sensitivity of these ultrathin supramolecular layers.

Electrochemistry. The electrochemical behavior of $PTCDI_2$ was investigated by cyclic voltammetry (CV) in a CH_3CN solution. The cyclic voltammogram is shown in Figure 7a, with additional details summarized in Table S1. In the case of $PTCDI_2$, we observed five quasireversible processes associated with both oxidation and reduction. The first oxidation process occurred at 212 mV, while the first reduction process was observed at −182 mV. Hence, $PTCD^{2+}$ is capable of producing both cation- and anion-radical species, which is highly advantageous for material applications. In comparison, (2,6-diisopropylphenyl)-3,4-perylenedicarboxylic imide demonstrates oxidation at 1.37 V (vs SCE) and reductions at −1.10 and −1.66 V (vs SCE).[72] More comprehensive information about electrochemical properties of different NDI molecules/complexes can be found elsewhere.[73−75] In terms of materials preparation, it is worth noting the synthesis of cation-radical salts through the electrochemical oxidation of perylene dyes.[76−79] The I^-/I_2 couple potential is 0.638 V (at 0 ionic strength and CH_3CN).[80]

The CV data for paste electrodes containing **2** and **3** are presented in Figure 7b,c, respectively. The paste composition calculated on a dry substance for complexes **2** and **3** is as follows: carbon powder: electroactive substance: Nafion (10%) water dispersion = 100:10:4 mg and 101.3:9.8:4.6 mg, respectively. These measurements were performed in a 0.1 M Bu_4NPF_6 acetonitrile solution at a 20 mV/s scan rate; additional details are summarized in Tables S2 and S3.

The frontier orbital energies for $PTCD^{2+}$ were determined based on the CV data. The HOMO energy level of $PTCD^{2+}$ was estimated to be −4.1 eV using the recorded oxidation onset potential [E_{Ox}(onset) = −0.27 V] and the oxidation potential of ferrocene [$E_{1/2}$(ferrocene) = 0.43 V). This estimation was performed using the equation: $E_{HOMO} = [(E_{Ox}(\text{onset}) - E_{1/2}(\text{ferrocene})) + 4.8]$ eV, taking the energy level of ferrocene/ferrocenium as 4.8 eV. The LUMO energy level was estimated to be −3.75 eV from the reduction onset potential [E_{Ox}(onset) = −0.62 V] according to the equation: $E_{LUMO} = [(E_{Red}(\text{onset}) - E_{1/2}(\text{ferrocene})) + 4.8]$ eV.

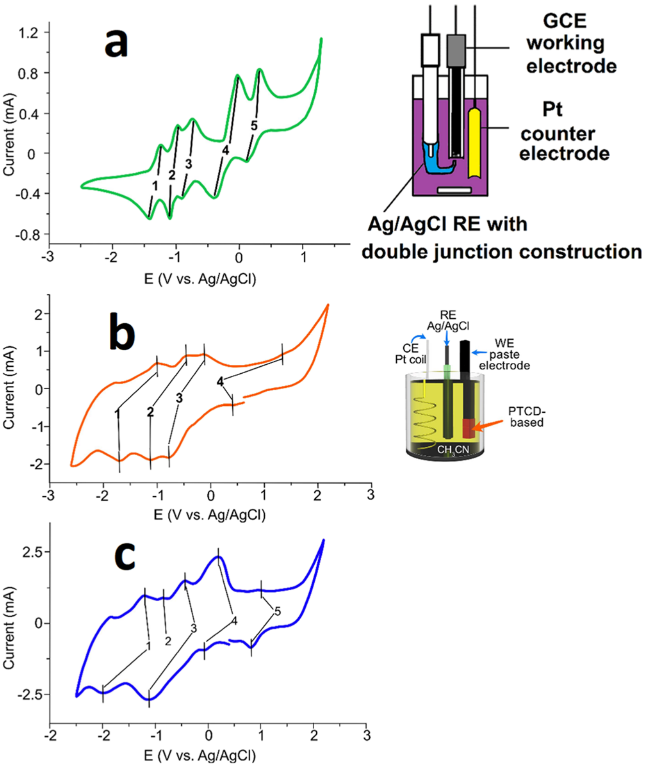

Figure 7. (a) CV data for $PTCDI_2$ in CH_3CN solution; (b) CV of the paste electrode containing $(PTCD)_3[PW_{12}O_{40}]_2\cdot 3DMSO\cdot 2H_2O$ (**2**); and (c) CV of the paste electrode containing $(PTCD)_2[SiW_{12}O_{40}]\cdot DMSO\cdot 2H_2O$ (**3**).

The HOMO energy level for both $[SiW_{12}O_{40}]^{4-}$ and $[PW_{12}O_{40}]^{3-}$ is −8.0 eV, while the LUMO levels are −4.5 and −4.6 eV, respectively.[5] This indicates that the incorporation of the $PTCD^{2+}$ cation and the POM anion results in a decrease of the LUMO level below −3.9 eV. The calculated values of HOMO/LUMO levels for $H_2BDMPy\text{-}Br_2NDI$ and $H_2BDMPy\text{-}I_2NDI$ using the B3LYP/LANL2DZ method are −6.68/−4.37 eV and −6.62/−4.18 eV, respectively.[30] Thus, in our case, the energy transfer is expected to be similar to that of the $H_2BDMPy\text{-}I_2NDI$-based hybrid and different from that of the bromine derivative. An important observation is that both complex **2** and complex **3** can be multiple times reversibly reduced but only oxidized once, suggesting their potential use as electron reservoirs in charge transfer systems. Bond et al. reported careful electrochemical studies of $[PW_{12}O_{40}]^{3-}$ and $[SiW_{12}O_{40}]^{4-}$ anions under different conditions.[81] In CH_3CN (0.1 M Bu_4NPF_6) $[PW_{12}O_{40}]^{3-}$ can be electrochemically reduced to 7− charge state at the following potentials: −669 (3−/4−), −1186 (4−/5−), −1894 (5−/6−), −2397 (6−/7−) mV. The same (0.1 Bu_4NClO_4 in CH_3CN) for $[SiW_{12}O_{40}]^{4-}$ can be done at potentials: −1140 (4−/5−), −1615 (5−/6−), −2280 (6−/7−) mV.

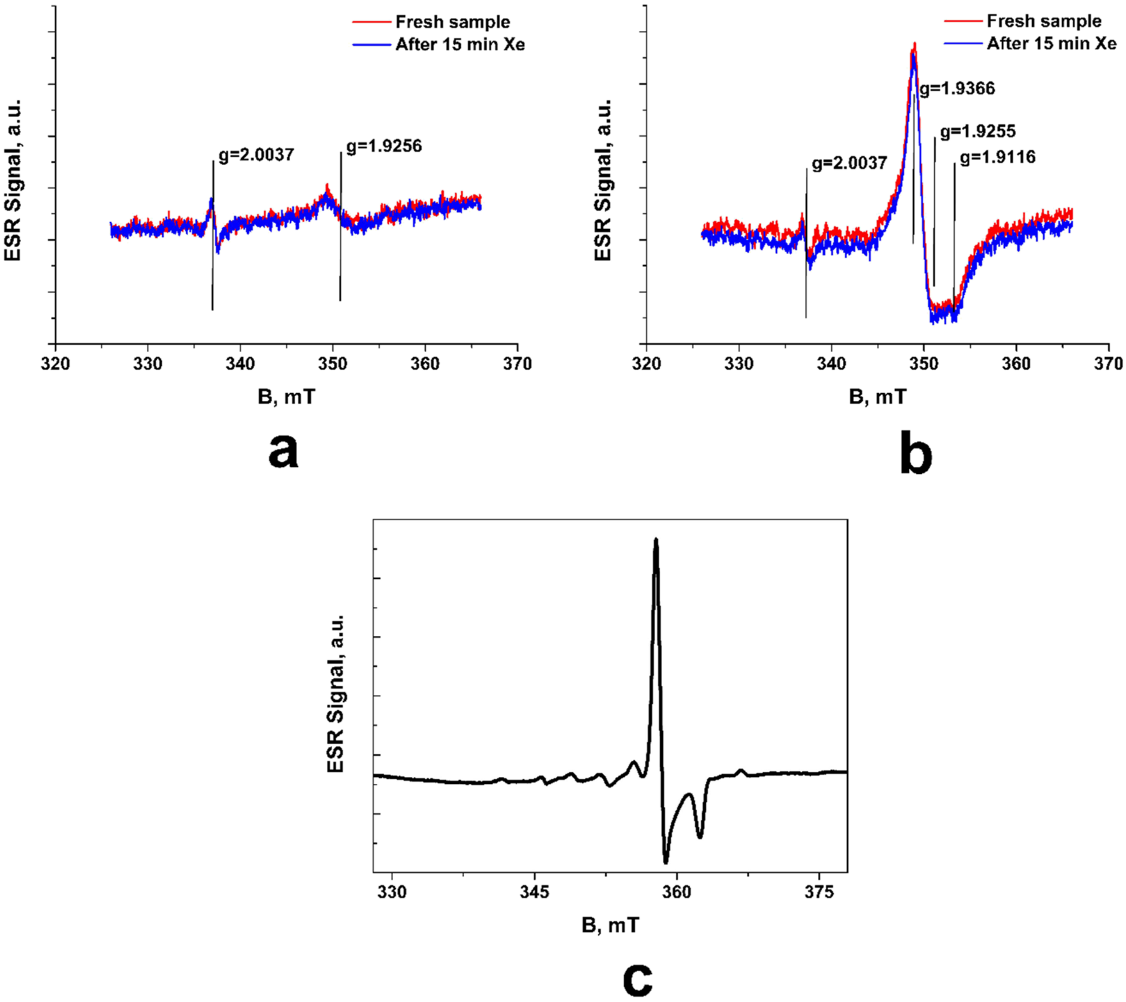

Figure 8. (a) ESR spectrum of solid **3** (red curve, room temperature for a fresh sample without degassing), and for the same sample after 15 min of irradiation with a focused full spectrum beam of a 150 W Xe lamp (blue curve); (b) ESR spectrum of solid **2** (red curve, room temperature for a fresh sample without degassing) and for the same sample after 15 min of irradiation with focused full spectrum beam of a 150 W Xe lamp (blue curve); (c) ESR spectrum of solid **2** in the region of the high-field group of lines at 100 K.

Electron Spin Resonance (ESR). ESR studies were conducted on solid samples of hybrid salts **2** and **3** to investigate whether they undergo intramolecular charge transfer, resulting in a reduced POM anion. Various experiments were performed, including temperature cycling in the range of 15−343 K, with and without air removal, and additional irradiation with a full spectrum of a 150 W Xe lamp to assess possible photochromic effects.

Figure 8a,b show the spectra of **2** and **3** recorded at room temperature. Both spectra feature a weak line in the region of "organic" g-values of about 2.0037, which originates from the samples themselves and is not an experimental artifact. Additionally, for sample **2**, a distinctive set of lines with lower g-values in the region typical for metal ions is observed, indicating the presence of the expected reduced POM anion (Figure S15). In contrast, only a single, much weaker line is observed for sample **3** in this region. The spectra of both samples remain unaffected by additional UV−visible light irradiation regardless of the presence or absence of air. An example of such spectra after a round of irradiation is shown in the same figure panels. The only noticeable effect of air removal is a slight narrowing of the "organic" line, which was expected as an indication of the signal connection to some surface sites. Subsequent experiments focused only on sample **2** as sample **3** did not yield any significant signals of interest.

Figure 8c shows the evolution of the higher field group of lines for complex **2** as it is cooled to 100 K. The spectrum assumes a typical axial shape with a well-resolved hyperfine structure. Further evolution of the ESR spectrum for sample **2** upon cooling down to 15K is shown in Figure S16a. (The results of spectral processing are given in Figure S16b.) These results reveal a group of lines in the g ~1.93 region and the emergence of a new group of lines belonging to a rhombic center in the g ~1.83−1.78 region.

The interpretation of the ESR results for $[XW_{12}O_{40}]^{n-}$ POMs should begin with the lowest temperatures. The spectra that exhibit a group of lines with g values around 1.83, as shown in Figure 8c, have been extensively reported and reproduced in simulations in earlier studies of Keggin-type POMs at Kelvin temperatures.[82−85] These lines have been unequivocally attributed to the W^{5+} signal of the reduced polytungstates. The rhombic symmetry of the spectrum is due to significant spin−orbit coupling in the heavy 5d element, leading to a substantial and well-resolved g-tensor anisotropy. The absence of hyperfine substructure from the ^{183}W isotope (I = 1/2, natural abundance 14.3%) is explained by the delocalization over 12 equiv W sites, with dynamic processes contributing starting already at low Kelvin temperatures. The relaxation properties of heavy 5d elements are usually unfavorable for observing ESR signals at temperatures above several tens of Kelvin. Additionally, the W nucleus itself is not a convenient reporter of the reduction state of symmetric polytungstates at moderately low cryogenic temperatures, such as those relevant for potential applications under ambient conditions. However, the observation of such a signal in a specifically designed cryogenic experiment guarantees the presence of a reduced $[XW^{V}W_{11}{}^{VI}O_{40}]^{n-}$ Keggin-type anion.

The group of lines with g around 1.93, which has been occasionally attributed to W^{5+} sites[29,86,87] in reduced $[XW_{12}O_{40}]^{n-}$ POMs, has been conclusively identified as originating from unavoidable traces of Mo present in tungsten raw materials. These traces result in minor $[XMoW_{11}O_{40}]^{n-}$ impurities in nominally pure polytungstates.[88]

At room temperature, the ESR spectrum of complex **2** is dominated by a broad line centered at g = 2.25 with a peak-to-peak width of about 100 mT (Figure S17a). This broad line overlaps with the signal from Mo^{5+} (g = 1.94) at the high-field minimum (Figure S17b). Interestingly, the intensity of the broad line, estimated from the second integral of the ESR spectrum, is several thousand times higher than that from Mo^{5+}, suggesting that it does not originate from impurities in **2**.

Upon cooling, the broad signal weakens and ultimately disappears at 15K. This behavior indicates that the broad line corresponds to the thermally populated excited state of **2** with a nonzero electron spin. A similar behavior was observed in metal−organic frameworks containing Cu_2 units.[89]

The ESR results indicate the presence of one-electron-reduced Keggin anions in the samples studied. It is important to note that these reduced anions were not intentionally prepared or generated through external means, unlike previous studies in which deliberate electrochemical, photochemical, or chemical reduction methods were employed. In the case of complex **2,** the reduction process seems to be spontaneous and is likely a result of intramolecular charge transfer from the organic cations with extended π-systems to the POM anion. Furthermore, the resulting state is surprisingly stable.

The ESR studies conducted over a span of one year and a half consistently yielded the same results. The initial sample was repeatedly tested through various manipulations, including thermocycling over extended temperature ranges, light irradiation, air exposure, and air removal, and the ESR signal observed in the first experiment persisted unchanged throughout all of these manipulations. Additionally, several more samples were prepared from the original batch, and freshly prepared batches consistently reproduced the ESR signal. These findings strongly support the observation of a genuine intramolecular POM reduction in this case.

Furthermore, the comparison with ESR studies of $(H_4BDMPy\text{-}Br_2NDI)[HPW_{12}O_{40}]\cdot 4NMP$ and $(H_4BDMPy\text{-}I_2NDI)[HPW_{12}O_{40}]$ indicates that the nature of the excited state based on cation-radical and POM-radical species formation is similar across these systems.[30] This highlights the importance of understanding the dynamics and properties of these excited states in the context of hybrid materials and their potential applications. One of the most prospective fields of polyoxometalate use is the charge transfer systems. Much research was done on the use of various POMs in the preparation of charge transfer salts.[90−92] This work takes us a step beyond by demonstrating a new hybrid combination with intriguing charge transfer properties.

■ CONCLUSIONS

We prepared new organic−inorganic hybrid salts based on Keggin-type POM and perylene diimide-based cations. These compounds demonstrated exceptional electrochemical behavior, including multistep reduction processes of both POM and cation-centered components. This makes them promising candidates for the development of charge storage systems and other applications, such as redox catalysis, capacitors, and memory devices.

The Raman spectroscopy analyses showed that the micro-aggregates in the solid phase possess a large degree of $\pi-\pi$ stacking, with AFM showing that these aggregates span different sizes and microstructures from particles to molecular self-assembled layers on graphite. Photoluminescence results showed no quenching in the solid state, which we attribute to the noncovalent mediation of polyoxometalate Keggin salt.

The ESR experiments provided evidence for the presence of paramagnetic centers associated with single-electron-reduced POM species at room temperature. Full charge separation occurred as the temperature decreased. Interestingly, the PL luminescence behavior is unaffected by the charge separation process, indicating that the formation of radicals in the bulk sample did not affect the luminescence centers.

The structural dualism observed between NDI and PDI derivatives in their respective hybrid salts provides insights into the weak cation−anion interactions induced by electrostatic or charge transfer effects. Controlling the π-system size of the organic cations allows manipulation of the different association effects in both the solid state and solution. This strategy opens new possibilities for the design and synthesis of soft-matter-based materials with tailored properties.

■ ASSOCIATED CONTENT

Supporting Information

The Supporting Information is available free of charge at https://pubs.acs.org/doi/10.1021/acs.inorgchem.3c03030.

Experimental, structural, electrochemical, ESR, and X-ray luminescence data (PDF)

Accession Codes

CCDC 2093314 contains the supplementary crystallographic data for this paper. These data can be obtained free of charge via www.ccdc.cam.ac.uk/data_request/cif, or by emailing data_request@ccdc.cam.ac.uk, or by contacting The Cambridge Crystallographic Data Centre, 12 Union Road, Cambridge CB2 1EZ, UK; fax: +44 1223 336033.

■ AUTHOR INFORMATION

Corresponding Author

Pavel A. Abramov − *Nikolaev Institute of Inorganic Chemistry SB RAS, Novosibirsk 630090, Russia; Research School of Chemistry and Applied Biomedical Sciences, Tomsk Polytechnic University, Tomsk 634034, Russia;* orcid.org/0000-0003-4479-5100; Email: abramov@niic.nsc.ru

Authors

Victoria G. Popova − *Nikolaev Institute of Inorganic Chemistry SB RAS, Novosibirsk 630090, Russia; Novosibirsk State University, Novosibirsk 630090, Russia*

Leonid V. Kulik − *Voevodsky Institute of Chemical Kinetics and Combustion SB RAS, Novosibirsk 630090, Russia;* orcid.org/0000-0001-8677-4418

Rimma I. Samoilova − *Voevodsky Institute of Chemical Kinetics and Combustion SB RAS, Novosibirsk 630090, Russia*

Dmitri V. Stass − *Voevodsky Institute of Chemical Kinetics and Combustion SB RAS, Novosibirsk 630090, Russia; Novosibirsk State University, Novosibirsk 630090, Russia*

Vasily V. Kokovkin − *Nikolaev Institute of Inorganic Chemistry SB RAS, Novosibirsk 630090, Russia*

Evgeni M. Glebov − *Voevodsky Institute of Chemical Kinetics and Combustion SB RAS, Novosibirsk 630090, Russia;* orcid.org/0000-0003-2683-4954

Alexey S. Berezin − *Nikolaev Institute of Inorganic Chemistry SB RAS, Novosibirsk 630090, Russia;* orcid.org/0000-0001-7436-8041

Alexander S. Novikov − *Institute of Chemistry, Saint Petersburg State University, Saint Petersburg 199034, Russia; Research Institute of Chemistry, Peoples' Friendship University of Russia (RUDN University), Moscow 117198, Russia;* orcid.org/0000-0001-9913-5324

Aura Garcia − *Research School of Chemistry and Applied Biomedical Sciences, Tomsk Polytechnic University, Tomsk 634034, Russia*

Hoang Tran Tuan − *Research School of Chemistry and Applied Biomedical Sciences, Tomsk Polytechnic University, Tomsk 634034, Russia*

Raul D. Rodriguez − *Research School of Chemistry and Applied Biomedical Sciences, Tomsk Polytechnic University, Tomsk 634034, Russia;* orcid.org/0000-0003-4016-1469

Maxim N. Sokolov − *Nikolaev Institute of Inorganic Chemistry SB RAS, Novosibirsk 630090, Russia;* orcid.org/0000-0001-9361-4594

Complete contact information is available at:
https://pubs.acs.org/10.1021/acs.inorgchem.3c03030

Author Contributions

The manuscript was written through contributions of all authors. All authors have given approval to the final version of the manuscript. V.G.P. − investigation (synthesis, characterization), L.V.K. − investigation (ESR), R.I.S. − investigation (ESR), D.V.S. − investigation (ESR, X-ray luminescence), V.V.K. − investigation (electrochemistry), E.M.G. − investigation (diffuse reflectance), A.S.B. − investigation (luminescence), A.S.N. − investigation (quantum-chemical calculations), A.S.G.B. − investigation (Raman spectroscopy), H.T.T. − investigation (Raman spectroscopy), R.D.R. − investigation (Raman spectroscopy), writing−review and editing; M.N.S. − writing−review and editing, P.A.A. − writing−original draft, project administration.

Funding

The NIIC team thanks the Ministry of Science and Higher Education of the Russian Federation for the access to luminescence and analytical equipment. The Raman and AFM investigations were supported by Priority 2030-NIP/extraSP-096-375-2023. A.S.N. is grateful to the RUDN University Strategic Academic Leadership Program for support of quantum-chemical calculations.

Notes

The authors declare no competing financial interest.

ACKNOWLEDGMENTS

The authors thank T.S. Sukhikh for providing the data collected at the XRD Facility of NIIC SB RAS, N.B. Kompankov (NIIC SB RAS) for NMR data collection and V.R. Shayapov (NIIC SB RAS) for band gap studies. The authors thank Miss Anna Mukhacheva for the GA preparation. AG thanks financial support by TPU Priority 2030-NIP/extraSP-096-375-2023.

REFERENCES

(1) Vasilopoulou, M.; Fakharuddin, A.; Coutsolelos, A. G.; Falaras, P.; Argitis, P.; Yusoff, A. R. Bin M.; Nazeeruddin, M. K. Molecular Materials as Interfacial Layers and Additives in Perovskite Solar Cells. *Chem. Soc. Rev.* **2020**, *49* (13), 4496−4526.

(2) Palilis, L. C.; Vasilopoulou, M.; Verykios, A.; Soultati, A.; Polydorou, E.; Argitis, P.; Davazoglou, D.; Yusoff, A. R. Bin M.; Nazeeruddin, M. K. Inorganic and Hybrid Interfacial Materials for Organic and Perovskite Solar Cells. *Adv. Energy Mater.* **2020**, *10* (27), No. 2000910.

(3) Sharma, K.; Sharma, V.; Sharma, S. S. Dye-Sensitized Solar Cells: Fundamentals and Current Status. *Nanoscale Res. Lett.* **2018**, *13* (1), 381.

(4) Yin, Z.; Wei, J.; Zheng, Q. Interfacial Materials for Organic Solar Cells: Recent Advances and Perspectives. *Adv. Sci.* **2016**, *3* (8), No. 1500362.

(5) Vasilopoulou, M.; Douvas, A. M.; Palilis, L. C.; Kennou, S.; Argitis, P. Old Metal Oxide Clusters in New Applications: Spontaneous Reduction of Keggin and Dawson Polyoxometalate Layers by a Metallic Electrode for Improving Efficiency in Organic Optoelectronics. *J. Am. Chem. Soc.* **2015**, *137* (21), 6844−6856.

(6) Chen, Y.; Wang, S.; Xue, L.; Zhang, Z.; Li, H.; Wu, L.; Wang, Y.; Li, F.; Zhang, F.; Li, Y. Insights into the Working Mechanism of Cathode Interlayers in Polymer Solar Cells via [(C8H17)4N]4-[SiW12O40]. *J. Mater. Chem. A* **2016**, *4* (48), 19189−19196.

(7) Tountas, M.; Topal, Y.; Verykios, A.; Soultati, A.; Kaltzoglou, A.; Papadopoulos, T. A.; Auras, F.; Seintis, K.; Fakis, M.; Palilis, L. C.; Tsikritzis, D.; Kennou, S.; Fakharuddin, A.; Schmidt-Mende, L.; Gardelis, S.; Kus, M.; Falaras, P.; Davazoglou, D.; Argitis, P.; Vasilopoulou, M. A Silanol-Functionalized Polyoxometalate with Excellent Electron Transfer Mediating Behavior to ZnO and TiO2 Cathode Interlayers for Highly Efficient and Extremely Stable Polymer Solar Cells. *J. Mater. Chem. C* **2018**, *6* (6), 1459−1469.

(8) Soultati, A.; Verykios, A.; Speliotis, T.; Fakis, M.; Sakellis, I.; Jaouani, H.; Davazoglou, D.; Argitis, P.; Vasilopoulou, M. Organic Solar Cells of Enhanced Efficiency and Stability Using Zinc Oxide:Zinc Tungstate Nanocomposite as Electron Extraction Layer. *Org. Electron.* **2019**, *71*, 227−237.

(9) Kang, Q.; Zu, Y.; Liao, Q.; Zheng, Z.; Yao, H.; Zhang, S.; He, C.; Xu, B.; Hou, J. An Inorganic Molecule-Induced Electron Transfer Complex for Highly Efficient Organic Solar Cells. *J. Mater. Chem. A* **2020**, *8* (11), 5580−5586.

(10) Chen, L.; Chen, W.-L.; Wang, X.-L.; Li, Y.-G.; Su, Z.-M.; Wang, E.-B. Polyoxometalates in Dye-Sensitized Solar Cells. *Chem. Soc. Rev.* **2019**, *48* (1), 260−284.

(11) Zhang, L.; Chen, Z. Polyoxometalates: Tailoring Metal Oxides in Molecular Dimension toward Energy Applications. *Int. J. Energy Res.* **2020**, *44*, 3316.

(12) Nishimoto, Y.; Yokogawa, D.; Yoshikawa, H.; Awaga, K.; Irle, S. Super-Reduced Polyoxometalates: Excellent Molecular Cluster Battery Components and Semipermeable Molecular Capacitors. *J. Am. Chem. Soc.* **2014**, *136* (25), 9042−9052.

(13) Streb, C.; Kastner, K.; Tucher, J. 13 Polyoxometalates in Photocatalysis. In *Chemical Photocatalysis*; De Gruyter, 2013; pp 247−262.

(14) Costa-Coquelard, C.; Sorgues, S.; Ruhlmann, L. Photocatalysis with Polyoxometalates Associated to Porphyrins under Visible Light: An Application of Charge Transfer in Electrostatic Complexes. *J. Phys. Chem. A* **2010**, *114* (22), 6394−6400.

(15) Dolbecq, A.; Mialane, P.; Keita, B.; Nadjo, L. Polyoxometalate-Based Materials for Efficient Solar and Visible Light Harvesting: Application to the Photocatalytic Degradation of Azo Dyes. *J. Mater. Chem.* **2012**, *22* (47), 24509.

(16) Li, N.; Liu, J.; Dong, B.; Lan, Y. Polyoxometalate-Based Compounds for Photo- and Electrocatalytic Applications. *Angew. Chem., Int. Ed.* **2020**, *59* (47), 20779−20793.

(17) Liao, J.-Z.; Wu, C.; Wu, X.-Y.; Deng, S.-Q.; Lu, C.-Z. Exceptional Photosensitivity of a Polyoxometalate-Based Charge-Transfer Hybrid Material. *Chem. Commun.* **2016**, *52* (46), 7394−7397.

(18) Busche, C.; Vilà-Nadal, L.; Yan, J.; Miras, H. N.; Long, D.-L.; Georgiev, V. P.; Asenov, A.; Pedersen, R. H.; Gadegaard, N.; Mirza, M. M.; Paul, D. J.; Poblet, J. M.; Cronin, L. Design and Fabrication of Memory Devices Based on Nanoscale Polyoxometalate Clusters. *Nature* **2014**, *515* (7528), 545−549.

(19) Bonchio, M.; Syrgiannis, Z.; Burian, M.; Marino, N.; Pizzolato, E.; Dirian, K.; Rigodanza, F.; Volpato, G. A.; La Ganga, G.; Demitri, N.; Berardi, S.; Amenitsch, H.; Guldi, D. M.; Caramori, S.; Bignozzi, C. A.; Sartorel, A.; Prato, M. Hierarchical Organization of Perylene Bisimides and Polyoxometalates for Photo-Assisted Water Oxidation. *Nat. Chem.* **2019**, *11* (2), 146−153.

(20) Tountas, M.; Topal, Y.; Polydorou, E.; Soultati, A.; Verykios, A.; Kaltzoglou, A.; Papadopoulos, T. A.; Auras, F.; Seintis, K.; Fakis, M.; Palilis, L. C.; Tsikritzis, D.; Kennou, S.; Koutsoureli, M.; Papaioannou, G.; Ersöz, M.; Kus, M.; Falaras, P.; Davazoglou, D.; Argitis, P.; Vasilopoulou, M. Low Work Function Lacunary Polyoxometalates as Electron Transport Interlayers for Inverted Polymer Solar Cells of Improved Efficiency and Stability. *ACS Appl. Mater. Interfaces* **2017**, *9* (27), 22773−22787.

(21) Douvas, A. M.; Tsikritzis, D.; Tselios, C.; Haider, A.; Mougharbel, A. S.; Kortz, U.; Hiskia, A.; Coutsolelos, A. G.; Palilis, L. C.; Vasilopoulou, M.; Kennou, S.; Argitis, P. Multi-Electron Reduction of Wells−Dawson Polyoxometalate Films onto Metallic, Semiconducting and Dielectric Substrates. *Phys. Chem. Chem. Phys.* **2019**, *21* (1), 427−437.

(22) Ling, Q.-H.; Zhu, J.-L.; Qin, Y.; Xu, L. Naphthalene Diimide- and Perylene Diimide-Based Supramolecular Cages. *Mater. Chem. Front.* **2020**, *4* (11), 3176−3189.

(23) Feng, J.; Jiang, W.; Wang, Z. Synthesis and Application of Rylene Imide Dyes as Organic Semiconducting Materials. *Chem. - An Asian J.* **2018**, *13* (1), 20−30.

(24) Gsänger, M.; Bialas, D.; Huang, L.; Stolte, M.; Würthner, F. Organic Semiconductors Based on Dyes and Color Pigments. *Adv. Mater.* **2016**, *28* (19), 3615−3645.

(25) Al Kobaisi, M.; Bhosale, S. V.; Latham, K.; Raynor, A. M.; Bhosale, S. V. Functional Naphthalene Diimides: Synthesis, Properties, and Applications. *Chem. Rev.* **2016**, *116* (19), 11685−11796.

(26) Zhan, X.; Facchetti, A.; Barlow, S.; Marks, T. J.; Ratner, M. A.; Wasielewski, M. R.; Marder, S. R. Rylene and Related Diimides for Organic Electronics. *Adv. Mater.* **2011**, *23* (2), 268−284.

(27) Liao, J.-Z.; Dui, X.-J.; Zhang, H.-L.; Wu, X.-Y.; Lu, C.-Z. Polyoxometalate Anion−π Interaction-Directed Assembly of a Three-Dimensional Hydrogen-Bonded Supramolecular Framework with Nanoscale Porosity. *CrystEngComm* **2014**, *16* (46), 10530−10533.

(28) Liao, J.-Z.; Wu, X.-Y.; Yong, J.-P.; Zhang, H.-L.; Yang, W.-B.; Yu, R.; Lu, C.-Z. Anion−π Interaction-Directed Assembly of Polyoxometalate-Based Host−Guest Compounds and Its Contribution to Photochromism. *Cryst. Growth Des.* **2015**, *15* (10), 4952−4958.

(29) You, M.-H.; Li, M.-H.; Di, Y.-M.; Wang, Y.-W.; Lin, M.-J. Switching on Room-Temperature Phosphorescence of Photochromic Hybrid Heterostructures by Anion-π Interactions. *Dye. Pigment.* **2020**, *173*, No. 107943.

(30) Di, Y.-M.; Li, M.-H.; You, M.-H.; Zhang, S.-Q.; Lin, M.-J. Photochromic and Room Temperature Phosphorescent Donor−Acceptor Hybrid Crystals Regulated by Core-Substituted Naphthalenediimides. *Inorg. Chem.* **2021**, *60* (21), 16233−16240.

(31) Liu, J.-J.; Fu, J.-J.; Liu, T.; Cheng, F.-X. Photochromic Polyoxometalate/Naphthalenediimide Hybrid Structure with Visible-Light-Driven Dye Degradation. *J. Solid State Chem.* **2022**, *312*, No. 123236.

(32) Zhao, J.-L.; Li, M.-H.; Cheng, Y.-M.; Zhao, X.-W.; Xu, Y.; Cao, Z.-Y.; You, M.-H.; Lin, M.-J. Photochromic Crystalline Hybrid Materials with Switchable Properties: Recent Advances and Potential Applications. *Coord. Chem. Rev.* **2023**, *475*, No. 214918.

(33) Abramov, P. A.; Novikov, A. S.; Sokolov, M. N. Interactions of Aromatic Rings in the Crystal Structures of Hybrid Polyoxometalates and Ru Clusters. *CrystEngComm* **2021**, *23* (36), 6409−6417.

(34) Politzer, P.; Murray, J. S.; Clark, T. Halogen Bonding and Other σ-Hole Interactions: A Perspective. *Phys. Chem. Chem. Phys.* **2013**, *15* (27), 11178.

(35) Murray, J. S.; Lane, P.; Politzer, P. Expansion of the σ-Hole Concept. *J. Mol. Model.* **2009**, *15* (6), 723−729.

(36) Wang, H.; Wang, W.; Jin, W. J. σ-Hole Bond vs π-Hole Bond: A Comparison Based on Halogen Bond. *Chem. Rev.* **2016**, *116* (9), 5072−5104.

(37) Clark, T.; Hennemann, M.; Murray, J. S.; Politzer, P. Halogen Bonding: The σ-Hole. *J. Mol. Model.* **2007**, *13* (2), 291−296.

(38) Chupina, A. V.; Shayapov, V.; Novikov, A. S.; Volchek, V. V.; Benassi, E.; Abramov, P. A.; Sokolov, M. N. [{AgL}2Mo8O26]n− Complexes: A Combined Experimental and Theoretical Study. *Dalt. Trans.* **2020**, *49* (5), 1522−1530.

(39) Fotović, L.; Bedeković, N.; Stilinović, V. Keggin-Type Anions as Halogen Bond Acceptors. *Cryst. Growth Des.* **2023**, *23* (5), 3384−3392.

(40) Kim, I.; Haverinen, H. M.; Wang, Z.; Madakuni, S.; Li, J.; Jabbour, G. E. Effect of Molecular Packing on Interfacial Recombination of Organic Solar Cells Based on Palladium Phthalocyanine and Perylene Derivatives. *Appl. Phys. Lett.* **2009**, *95* (2), No. 023305.

(41) Wu, N.; Zhang, Y.; Wang, C.; Slattum, P. M.; Yang, X.; Zang, L. Thermoactivated Electrical Conductivity in Perylene Diimide Nanofiber Materials. *J. Phys. Chem. Lett.* **2017**, *8* (1), 292−298.

(42) Akamatu, H.; Inokuchi, H.; Matsunaga, Y. Electrical Conductivity of the Perylene−Bromine Complex. *Nature* **1954**, *173* (4395), 168−169.

(43) Inokuchi, H.; Kuroda, H.; Akamatu, H. On the Electrical Conductivity of the Organic Thin Films: Perylene, Coronene and Violanthrene. *Bull. Chem. Soc. Jpn.* **1961**, *34* (6), 749−753.

(44) Ali, S.; Gupta, A.; Shafiei, M.; Langford, S. J. Recent Advances in Perylene Diimide-Based Active Materials in Electrical Mode Gas Sensing. *Chemosensors* **2021**, *9* (2), 30.

(45) Geng, Y.; Li, H.-B.; Wu, S.-X.; Su, Z.-M. The Interplay of Intermolecular Interactions, Packing Motifs and Electron Transport Properties in Perylene Diimide Related Materials: A Theoretical Perspective. *J. Mater. Chem.* **2012**, *22* (39), 20840.

(46) Coronado, E.; Galán-Mascarós, J. R.; Giménez-Saiz, C.; Gómez-García, C. J.; Martínez-Ferrero, E.; Almeida, M.; Lopes, E. B.; Capelli, S. C.; Llusar, R. M. New Conducting Radical Salts Based upon Keggin-Type Polyoxometalates and Perylene. *J. Mater. Chem.* **2004**, *14* (12), 1867−1872.

(47) Wu, W.; Liu, Y.; Zhu, D. π-Conjugated Molecules with Fused Rings for Organic Field-Effect Transistors: Design, Synthesis and Applications. *Chem. Soc. Rev.* **2010**, *39* (5), 1489−1502.

(48) Kim, S.-J.; Kim, T.-H.; Ahmad, I.; Noh, H.-J.; Jung, S.-M.; Im, Y.-K.; Mahmood, J.; Bae, Y.-S.; Baek, J.-B. Fused Aromatic Networks with the Different Spatial Arrangement of Structural Units. *Cell Reports Phys. Sci.* **2021**, *2* (7), No. 100502.

(49) Meyer, E. A.; Castellano, R. K.; Diederich, F. Interactions with Aromatic Rings in Chemical and Biological Recognition. *Angew. Chem., Int. Ed.* **2003**, *42* (11), 1210−1250.

(50) Huang, L.; Catalano, V. J.; Tam-Chang, S.-W. Anisotropic Fluorescent Materials via Self-Organization of Perylenedicarboximide. *Chem. Commun.* **2007**, 2016−2018.

(51) Liu, W.; Bobbala, S.; Stern, C. L.; Hornick, J. E.; Liu, Y.; Enciso, A. E.; Scott, E. A.; Stoddart, J. F. XCage: A Tricyclic Octacationic

Receptor for Perylene Diimide with Picomolar Affinity in Water. *J. Am. Chem. Soc.* **2020**, *142* (6), 3165−3173.

(52) Bader, R. F. W. A Quantum Theory of Molecular Structure and Its Applications. *Chem. Rev.* **1991**, *91* (5), 893−928.

(53) Ivanov, D. M.; Kirina, Y. V.; Novikov, A. S.; Starova, G. L.; Kukushkin, V. Y. Efficient π-Stacking with Benzene Provides 2D Assembly of Trans-[PtCl2(p-CF3C6H4CN)2]. *J. Mol. Struct.* **2016**, *1104*, 19−23.

(54) Rozhkov, A. V.; Novikov, A. S.; Ivanov, D. M.; Bolotin, D. S.; Bokach, N. A.; Kukushkin, V. Y. Structure-Directing Weak Interactions with 1,4-Diiodotetrafluorobenzene Convert One-Dimensional Arrays of [MII(Acac)2] Species into Three-Dimensional Networks. *Cryst. Growth Des.* **2018**, *18* (6), 3626−3636.

(55) Rozhkov, A. V.; Krykova, M. A.; Ivanov, D. M.; Novikov, A. S.; Sinelshchikova, A. A.; Volostnykh, M. V.; Konovalov, M. A.; Grigoriev, M. S.; Gorbunova, Y. G.; Kukushkin, V. Y. Reverse Arene Sandwich Structures Based upon Π-Hole···[MII] (D8M = Pt, Pd) Interactions, Where Positively Charged Metal Centers Play the Role of a Nucleophile. *Angew. Chem., Int. Ed.* **2019**, *58* (13), 4164−4168.

(56) Katkova, S. A.; Mikherdov, A. S.; Kinzhalov, M. A.; Novikov, A. S.; Zolotarev, A. A.; Boyarskiy, V. P.; Kukushkin, V. Y. (Isocyano Group Π-Hole)···[D-MII] Interactions of (Isocyanide)[MII] Complexes, in Which Positively Charged Metal Centers (D8-M = Pt, Pd) Act as Nucleophiles. *Chem. − Eur. J.* **2019**, *25* (36), 8590−8598.

(57) Baykov, S. V.; Filimonov, S. I.; Rozhkov, A. V.; Novikov, A. S.; Ananyev, I. V.; Ivanov, D. M.; Kukushkin, V. Y. Reverse Sandwich Structures from Interplay between Lone Pair−π-Hole Atom-Directed C···dz2 [M] and Halogen Bond Interactions. *Cryst. Growth Des.* **2020**, *20* (2), 995−1008.

(58) Mukhacheva, A. A.; Komarov, V. Y.; Kokovkin, V. V.; Novikov, A. S.; Abramov, P. A.; Sokolov, M. N. Unusual π−π Interactions Directed by the [{(C6H6)Ru}2W8O30(OH)2]6− Hybrid Anion. *CrystEngComm* **2021**, *23* (23), 4125−4135.

(59) Lukoyanov, A. N.; Fomenko, I. S.; Gongola, M. I.; Shul'pina, L. S.; Ikonnikov, N. S.; Shul'pin, G. B.; Ketkov, S. Y.; Fukin, G. K.; Rumyantcev, R. V.; Novikov, A. S.; Nadolinny, V. A.; Sokolov, M. N.; Gushchin, A. L. Novel Oxidovanadium Complexes with Redox-Active R-Mian and R-Bian Ligands: Synthesis, Structure, Redox and Catalytic Properties. *Molecules* **2021**, *26* (18), 5706.

(60) Baykov, S. V.; Mikherdov, A. S.; Novikov, A. S.; Geyl, K. K.; Tarasenko, M. V.; Gureev, M. A.; Boyarskiy, V. P. π−π Noncovalent Interaction Involving 1,2,4- and 1,3,4-Oxadiazole Systems: The Combined Experimental, Theoretical, and Database Study. *Molecules* **2021**, *26* (18), 5672.

(61) Espinosa, E.; Alkorta, I.; Elguero, J.; Molins, E. From Weak to Strong Interactions: A Comprehensive Analysis of the Topological and Energetic Properties of the Electron Density Distribution Involving X−H···F−Y Systems. *J. Chem. Phys.* **2002**, *117* (12), 5529−5542.

(62) Johnson, E. R.; Keinan, S.; Mori-Sánchez, P.; Contreras-García, J.; Cohen, A. J.; Yang, W.; Mori-Sánchez, P.; Contreras-García, J.; Cohen, A. J.; Yang, W. Revealing Noncovalent Interactions. *J. Am. Chem. Soc.* **2010**, *132* (18), 6498−6506.

(63) Contreras-García, J.; Johnson, E. R.; Keinan, S.; Chaudret, R.; Piquemal, J.-P.; Beratan, D. N.; Yang, W. NCIPLOT: A Program for Plotting Noncovalent Interaction Regions. *J. Chem. Theory Comput.* **2011**, *7* (3), 625−632.

(64) Kong, K.; Zhang, S.; Chu, Y.; Hu, Y.; Yu, F.; Ye, H.; Ding, H.; Hua, J. A Self-Assembled Perylene Diimide Nanobelt for Efficient Visible-Light-Driven Photocatalytic H2 Evolution. *Chem. Commun.* **2019**, *55* (56), 8090−8093.

(65) Zhang, F.; Ma, Y.; Chi, Y.; Yu, H.; Li, Y.; Jiang, T.; Wei, X.; Shi, J. Self-Assembly, Optical and Electrical Properties of Perylene Diimide Dyes Bearing Unsymmetrical Substituents at Bay Position. *Sci. Rep.* **2018**, *8* (1), 8208.

(66) Yang, J.; Miao, H.; Wei, Y.; Li, W.; Zhu, Y. π−π Interaction between Self-Assembled Perylene Diimide and 3D Graphene for Excellent Visible-Light Photocatalytic Activity. *Appl. Catal. B Environ.* **2019**, *240*, 225−233.

(67) Angelella, M.; Wang, C.; Tauber, M. J. Resonance Raman Spectra of a Perylene Bis(Dicarboximide) Chromophore in Ground and Lowest Triplet States. *J. Phys. Chem. A* **2013**, *117* (38), 9196−9204.

(68) Łapiński, A.; Graja, A.; Olejniczak, I.; Bogucki, A.; Połomska, M.; Baffreau, J.; Perrin, L.; Leroy-Lhez, S.; Hudhomme, P. Vibrational and Electronic Properties of Perylenediimide Linked to Fullerene and Tetrathiafulvalene. *Mol. Cryst. Liq. Cryst.* **2006**, *447* (1), 405−421.

(69) Lloret, V.; Nuin, E.; Kohring, M.; Wild, S.; Löffler, M.; Neiss, C.; Krieger, M.; Hauke, F.; Görling, A.; Weber, H. B.; Abellán, G.; Hirsch, A. Noncovalent Functionalization and Passivation of Black Phosphorus with Optimized Perylene Diimides for Hybrid Field Effect Transistors. *Adv. Mater. Interfaces* **2020**, *7* (23), No. 2001290.

(70) Zhang, B.; Lyskov, I.; Wilson, L. J.; Sabatini, R. P.; Manian, A.; Soleimaninejad, H.; White, J. M.; Smith, T. A.; Lakhwani, G.; Jones, D. J.; Ghiggino, K. P.; Russo, S. P.; Wong, W. W. H. FRET-Enhanced Photoluminescence of Perylene Diimides by Combining Molecular Aggregation and Insulation. *J. Mater. Chem. C* **2020**, *8* (26), 8953−8961.

(71) Taniguchi, A.; Kaji, D.; Hara, N.; Murata, R.; Akiyama, S.; Harada, T.; Sudo, A.; Nishikawa, H.; Imai, Y. Solid-State AIEnh-Circularly Polarised Luminescence of Chiral Perylene Diimide Fluorophores. *RSC Adv.* **2019**, *9* (4), 1976−1981.

(72) Lee, S. K.; Zu, Y.; Herrmann, A.; Geerts, Y.; Müllen, K.; Bard, A. J. Electrochemistry, Spectroscopy and Electrogenerated Chemiluminescence of Perylene, Terrylene, and Quaterrylene Diimides in Aprotic Solution. *J. Am. Chem. Soc.* **1999**, *121* (14), 3513−3520.

(73) Pasaogullari, N.; Icil, H.; Demuth, M. Symmetrical and Unsymmetrical Perylene Diimides: Their Synthesis Photophysical and Electrochemical Properties. *Dye. Pigment.* **2006**, *69* (3), 118−127.

(74) Wiebeler, C.; Vollbrecht, J.; Neuba, A.; Kitzerow, H.-S.; Schumacher, S. Unraveling the Electrochemical and Spectroscopic Properties of Neutral and Negatively Charged Perylene Tetraethylesters. *Sci. Rep.* **2021**, *11* (1), 16097.

(75) Chen, K.-Y.; Chang, C.-W. Highly Soluble Monoamino-Substituted Perylene Tetracarboxylic Dianhydrides: Synthesis, Optical and Electrochemical Properties. *Int. J. Mol. Sci.* **2014**, *15* (12), 22642−22660.

(76) Oyama, M.; Nitta, Y.; Okazaki, S. Anion-Controlled Electrocrystallization of Perylene Cation Radical Salts. *J. Electroanal. Chem.* **2001**, *511* (1−2), 88−93.

(77) Shine, H. J.; Ristagno, C. V. Ion Radicals. XXIII. Reactions of the Perylene Cation Radical. *J. Org. Chem.* **1971**, *36* (26), 4050−4055.

(78) Micheletto, R.; Matsui, J.; Yoshimatsu, N.; Oyama, M.; Okazaki, S. Study of the Fluorescence of Perylene Cation Radical Salts with a near Field Optical Setup. *Colloid Polym. Sci.* **2002**, *280* (12), 1067−1074.

(79) Ilakovac, V.; Ravy, S.; Moradpour, A.; Firlej, L.; Bernier, P. Disorder and Electronic Properties of Substituted Perylene Radical-Cation Salts. *Phys. Rev. B* **1995**, *52* (6), 4108−4122.

(80) Baucke, F. G. K.; Bertram, R.; Cruse, K. The Iodide-Iodine System in Acetonitrile. *J. Electroanal. Chem. Interfacial Electrochem.* **1971**, *32* (2), 247−256.

(81) Guo, S.-X.; Mariotti, A. W. A.; Schlipf, C.; Bond, A. M.; Wedd, A. G. A Systematic Approach to the Simulation of the Voltammetric Reduction of [α-SiW12O40]4− in Buffered Aqueous Electrolyte Media and Acetonitrile. *J. Electroanal. Chem.* **2006**, *591* (1), 7−18.

(82) Ueda, T.; Kodani, K.; Ota, H.; Shiro, M.; Guo, S.-X.; Boas, J. F.; Bond, A. M. Voltammetric and Spectroscopic Studies of α- and β-[PW12O40]3− Polyoxometalates in Neutral and Acidic Media: Structural Characterization as Their [(n-Bu4N)3][PW12O40] Salts. *Inorg. Chem.* **2017**, *56* (7), 3990−4001.

(83) Sanchez, C.; Livage, J.; Launay, J. P.; Fournier, M. Electron Delocalization in Mixed-Valence Tungsten Polyanions. *J. Am. Chem. Soc.* **1983**, *105* (23), 6817−6823.

(84) Prados, R. A.; Pope, M. T. Low-Temperature Electron Spin Resonance Spectra of Heteropoly Blues Derived from Some 1:12 and

2:18 Molybdates and Tungstates. *Inorg. Chem.* **1976**, *15* (10), 2547−2553.

(85) Bi, L.; Wang, E.; Xu, L.; Huang, R. Synthesis, Properties and Crystal Structure of Some Polyoxometallates Containing the Tris-(Hydroxymethyl)Aminomethane Cation. *Inorg. Chim. Acta* **2000**, *305* (2), 163−171.

(86) Saidhanov, S. S.; Kokorin, A. I.; Savinov, E. N.; Vokov, A. I.; Parmon, V. N. Changes in Catalytic Properties of 12-Heteropolyacids in Reaction of Dihydrogen Evolution from Water Induced by Their Immobilization on Anion-Exchange Polymers. *J. Mol. Catal.* **1983**, *21* (1−3), 365−373.

(87) Chen, D.; Sahasrabudhe, A.; Wang, P.; Dasgupta, A.; Yuan, R.; Roy, S. Synthesis and Properties of a Novel Quarternerized Imidazolium [α-PW12O40]3− Salt as a Recoverable Photo-Polymerization Catalyst. *Dalt. Trans.* **2013**, *42* (29), 10587.

(88) Fricke, R.; Jerschkewitz, H.-G.; Öhlmann, G. Electron Spin Resonance Studies of Free and Supported 12-Heteropoly Acids. Part 6.—The Investigation of Reduced H4(SiW12O40)·xH2O and Ag4(SiW12O40)·xH2O and the Effects of Oxygen Adsorption. *J. Chem. Soc. Faraday Trans. 1 Phys. Chem. Condens. Phases* **1987**, *83* (10), 3115.

(89) Šimėnas, M.; Kobalz, M.; Mendt, M.; Eckold, P.; Krautscheid, H.; Banys, J.; Pöppl, A. Synthesis, Structure, and Electron Paramagnetic Resonance Study of a Mixed Valent Metal−Organic Framework Containing Cu2 Paddle-Wheel Units. *J. Phys. Chem. C* **2015**, *119* (9), 4898−4907.

(90) Coronado, E.; Gómez-García, C. J. Polyoxometalate-Based Molecular Materials. *Chem. Rev.* **1998**, *98* (1), 273−296.

(91) Coronado, E.; Galán-Mascarós, J. R.; Giménez-Saiz, C.; Gómez-García, C. J.; Triki, S. Hybrid Molecular Materials Based upon Magnetic Polyoxometalates and Organic π-Electron Donors: Syntheses, Structures, and Properties of Bis(Ethylenedithio)-Tetrathiafulvalene Radical Salts with Monosubstituted Keggin Polyoxoanions. *J. Am. Chem. Soc.* **1998**, *120* (19), 4671−4681.

(92) Ouahab, L. The Polyoxometalates as Precursors in Molecular Materials. *C. R. Acad. Sci., Ser. IIC: Chem.* **1998**, *1* (5−6), 369−380.